35th European Modeling & Simulation Symposium
20th International Multidisciplinary Modeling & Simulation Multiconference

2724-0029 © 2023 The Authors.
doi: 10.46354/i3m.2023.emss.027

Data-driven modeling using convolutional neural network for experimental velocity fields of an impinging jet

Ali Mjalled[1], Mouhammad El Hassan[2*], Hassan H. Assoum[3] and Martin Mönnigmann[1]

[1]Ruhr University Bochum, Universitätsstraße 150, Bochum, 44801, Germany
[2]Prince Mohammad Bin Fahd University, Al Khobar, 31952, Saudi Arabia
[3]Beirut Arab University, Department of Mechanical Engineering, Tripoli, 1300, Lebanon

[*]Corresponding author. Email address: melhassan@pmu.edu.sa

Abstract

Modeling and analysis of complex flow behavior of impingement jets is a problem of significant importance in many engineering applications. Due to the nonlinear nature of these flows, traditional modeling methods often struggle to provide accurate representation of the flow features. Therefore, the goal of this work is to build a data-driven model for the available data to uncover the hidden features of the underlying dynamics, and to improve analysis and modeling of impinging jets. The available data consist of experimental velocimetry results of a circular impinging jet at a Reynolds number of 1260. The time-resolved particle image velocimetry (TR-PIV) technique was used to obtain velocity field data. An Autoencoder (AE) which is a special type of convolutional neural network is used for data compression and thus to learn the hidden features of the jet. The accuracy for reconstruction purposes was evaluated for various dimensions of the AE latent vector. According to the findings, the flow field image can be reconstructed using only one variable in the latent vector, which corresponds a reduction to 0.0015% in the size of the original flow image. The analysis of the spectral content of the AE variables revealed two primary frequency peaks, which coincided with those identified in the transverse velocity spectrum extracted from the main vortices' path. This suggests a connection between the AE variables and the vortical structures.

Keywords: Convolutional neural networks; Autoencoders; Impinging jet; PIV measurements

1. Introduction

Impinging jets have been extensively researched in the past 50 years due to their various industrial applications such as cooling of turbine blades, paper drying, annealing of glass, and more. Understanding vortex dynamics in different regions of the impinging jet is crucial both fundamentally and practically to study the heat transfer performance in such configurations. Many studies have been conducted to explore the physics of impinging jet flow (El Hassan et al., 2012, 2013) and analyze the importance of different flow parameters. Some studies have analyzed the flow field associated with jet impingement on a flat surface, including those conducted by (Fabris et al., 1996; Orlandi & Verzicco, 1993). A feedback phenomenon that controls high-speed subsonic impinging jets at the nozzle exit was found and studied by (Assoum et al., 2014; Assoum, Hamdi, Abed-Meraïm, El Hassan, Hammoud, et al., 2017; Assoum, Hamdi, Hassan, et al.,

2020). In solar energy technologies, solar collectors often face challenges such as overheating and inadequate heat transfer, which can limit their performance. To tackle this issue, cooling techniques, such as jet impingement cooling, have been proposed to enhance heat transfer rates and boost performance (Eng Ewe et al., 2022). Additionally, impinging jets have found applications in cooling electronic devices, including computer chips and power electronics. During operation, electronic devices generate heat, which can impair their performance and even cause damage if not dissipated effectively.

Describing and analyzing the fluid dynamics of flows such as those of impinging jets can be achieved using computational fluid dynamics (CFD) simulations or through experimental measurements. Due to the high cost associated with memory and CPU time, efficient reduced order models (ROMs) were developed for complex systems. ROM involves finding a low-dimensional approximation of high fidelity, where the high-fidelity data may be obtained either experimentally or numerically. The reduction is achieved by identifying a subspace that is defined by a small number of basic functions (typically around ten) on which the ROM is constructed. One common approach to finding the reduced space is proper orthogonal decomposition (POD) (Lumley, 1967) through singular value decomposition (SVD) of the high-fidelity data. The ROM is then defined by a linear combination of the most essential basis functions, with the associated coefficients referred to as reduced coefficients.

There are two main types of ROM techniques: intrusive and non-intrusive methods. In intrusive methods, the reduced coefficients are determined by solving ordinary differential equations after projecting the full order model (FOM) (Benner et al., 2015; Berner et al., 2020) onto the reduced space. On the other hand, non-intrusive methods approximate the reduced coefficients using a regression model without needing access to the governing equations of the FOM. Artificial neural networks have been shown to be effective regression models for non-intrusive methods.

For unsteady flows, Galerkin-projection ROMs have been developed in the intrusive context (Deane et al., 1991; John et al., 2010). Some of these studies have also developed parameter-dependent ROMs (Amsallem & Farhat, 2008), although these ROMs can sometimes be unstable and require post-processing fitting to the original data. Petrov-Galerkin is an alternative projection-based technique that can be used to develop more accurate and long-term stable ROMs (Reineking et al., 2022). Meanwhile, in non-intrusive methods, neural networks have emerged as a useful tool for predicting the temporal evolution of reduced coefficients (Pawar et al., 2019). Some authors have utilized long short-term memory (LSTM) neural networks in the non-intrusive framework (Maulik et al., 2021).

While experimental methods, such as particle image velocimetry (PIV), have improved our understanding about impinging jets, the underlying hidden feature dynamics is still not fully explored. This problem has been addressed using data-driven techniques, such as POD. However, POD is restricted to linear space approximation, which may not capture the nonlinear properties in these flows. Therefore, the aim of this study is to employ a non-intrusive neural network technique for nonlinear dimensionality reduction to further apprehend the flow dynamics of impinging jets. The autoencoder (AE) neural network technique was employed to learn the underlying characteristics of the jet and to reconstruct the flow. The accuracy of the reconstruction was evaluated for different dimensions of the AE latent vector, and its spectral content was displayed with transverse velocity at a location where the primary vortices of the flow pass.

The remainder of this paper is organized as follows. Section 2 introduces the experimental setup. In section 3, the data-driven model is presented. Section 4 presents the results obtained. Finally, conclusions are provided in section 5.

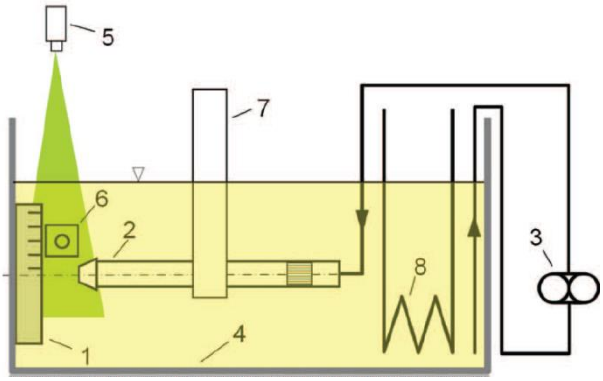

Figure 1. The experimental setup, which consists of several components. circular disk (1), cylindrical tube (2), pump (3), reservoir (4), laser head (5), camera (6), support (7), and cooling coil (8).

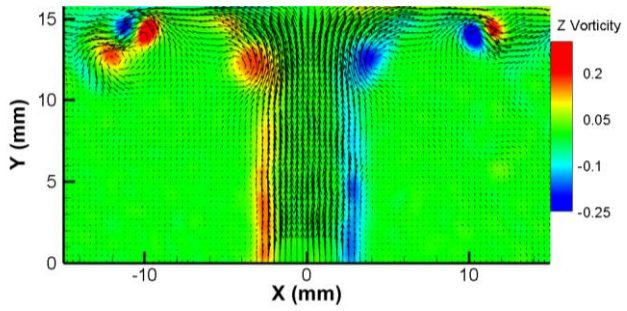

Figure 2. Snapshot of the derived vorticity.

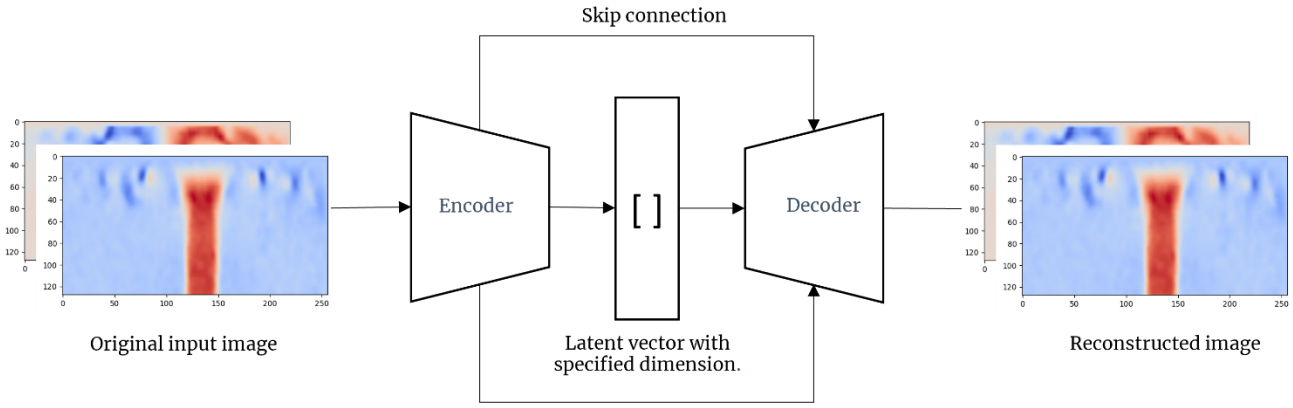

Figure 3. Autoencoder with U-net architecture.

2. Experimental data

In Fig. 1 the experimental setup that was designed for obtaining the two velocity components of an impinging jet using PIV is presented. The circular jet is generated by a nozzle fed with water from a reservoir using a gear pump. The water jet impinges on a circular disc with a fixed ratio of L/D = 2.08, where L is the nozzle to plate distance and D represents the jet exit diameter (D = 7.8 mm). The Reynolds number, based on D and the exit velocity, is Re = 1260. The PIV system consisted of a Nd:YLF NewWave Pegasus laser with a wavelength of 527 nm and 10 mJ energy, and a Phantom V9 camera with a resolution of 1200×1632 pixels^2. Small glass spheres measuring 9-13 μm in diameter were used as tracers for the PIV measurements. 500 pairs of images were acquired during 1 second. The camera and laser synchronization was established by a LaVision High-Speed Controller, and the acquired data was processed using DaVis 8.0 software. The final grid size used for processing the images comprised of 32×32-pixel size interrogation windows with 50% overlap, resulting in a spatial resolution of 0.65 mm. The longitudinal and transverse velocity components are referred to as Vy and Vx, respectively. The total error, which was obtained by accumulating the root mean square and bias errors, was found to be 3.7% of the mean axial velocity. Fig.2 shows a snapshot of the obtained measured velocity field and the derived vorticity.

3. Autoencoders for data-driven modeling

Fig. 3 shows the data driven model that is based on the convolutional AE. AEs are special type of neural networks used for data compression and thus they are suited well for learning hidden features in images. Essentially, they allow to find a compressed version of the image in an intermediate layer. This compressed representation is in general known as latent vector. Once the AE has been determined, it accepts as its input a flow field image and returns the reconstructed image as its output. More specifically, an AE consists of an encoder and decoder function. The encoder function f maps the input image X to the latent vector z, i.e.,

$$z = f(X), \tag{1}$$

while the decoder function reconstructs the original image given the latent vector z, i.e.,

$$X' = g(z) = g(f(X)). \tag{2}$$

The functions f and g are typically learned during the training phase of the AE by minimizing the loss function between the original image X and its reconstructed output X'. This process involves optimizing the network's parameters, i.e., weights and biases, in order to obtain the most accurate reconstruction of the input image. The AE utilized in this study is based on the U-Net architecture, which is designed with skip connections (see Fig. 3) to preserve important information between the encoder and decoder. This allows for more effective feature extraction and reconstruction of the input data.

The architecture of the encoder consists of six convolution layers parametrized with 64 filters each, except for the first and last convolutional layers, which are equipped with 32 and 16 filters, respectively. The size of the kernel used in all the convolutional layers is 4×4, and a stride of 2 is used in both spatial directions to reduce the dimensionality. Following every convolutional layer, a batch normalization layer is applied, accompanied with a leaky rectified linear unit (LeakyReLu) as activation function. The encoder path is terminated with a flattening layer to obtain the desired latent vector. The decoder path starts with a reshape layer to obtain the 3D tensorial format of the latent vector. It has the same symmetrical structure of the encoder, but with using the inverse counterpart mathematical operations, i.e., the convolution layer is replaces by convolutional transpose layer. The U-net structure is obtained by merging the intermediate outputs of the encoder with their corresponding counterparts in the decoder path. This merging process is accomplished using a concatenate layer, which is followed by a convolutional layer to adjust the dimensionality for further merging connections. The output layer of the decoder uses a sigmoid activation function to bound the predictions.

4. Results

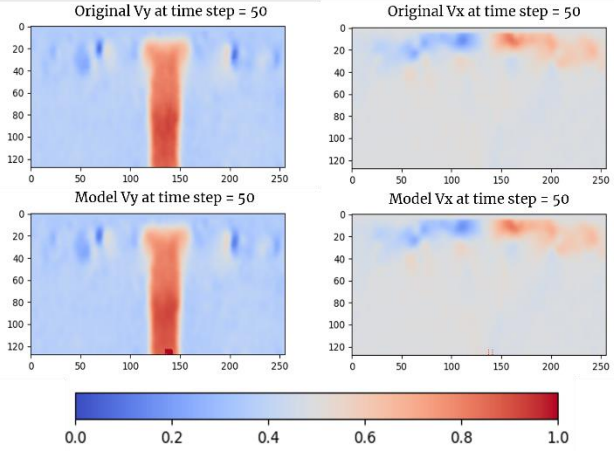

Figure 4. Comparison between the original flow image and the reconstructed image obtained using AE1 for the normalized Vy (left) and Vx (right). The results shown correspond to the image at time step 50.

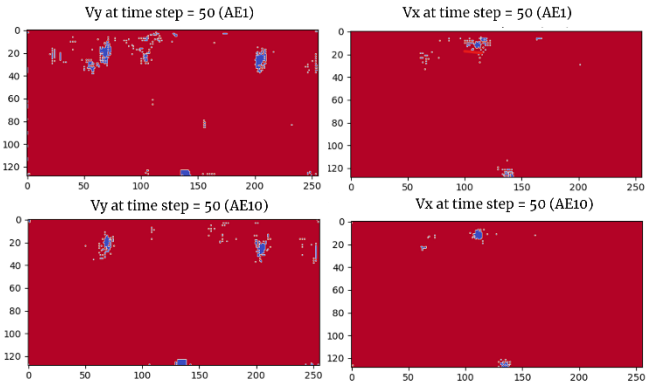

Figure 5. Matched pixels with 2% tolerance for AE1 (upper) and AE10 (lower) for Vy (left) and Vx (left). The results shown correspond to the image at time step 50. The pixels in red indicate that the relative prediction error in these locations is less than 2%.

The U-net AE presented in section 3 is trained using a dataset of 500 PIV snapshots. 20% of the frames are used to validate the model and prevent overfitting. The learning parameters of the AE are optimized by minimizing a mean squared error (MSE) loss function between the original and reconstructed images. For this purpose, we use Adam optimizer with learning rate 0.002 and batch size 32. The AE is trained for 210 epochs using an early stopping criterion. The accuracy of the AE is measured in terms of the similarity between X and X'. An ideal AE would obviously result in $X' = X$. In this case z is a perfect, lossless representation of X in the reduced space. For the evaluation of the AE, we compare the PIV images with the reconstructed output images produced by the AE.

The evaluation is in terms of the accuracy with respect to the number of matched pixels, i.e.,

$$\text{Accuracy} = \frac{\text{Number of matched pixels}}{\text{Number of all pixels}} \times 100.$$

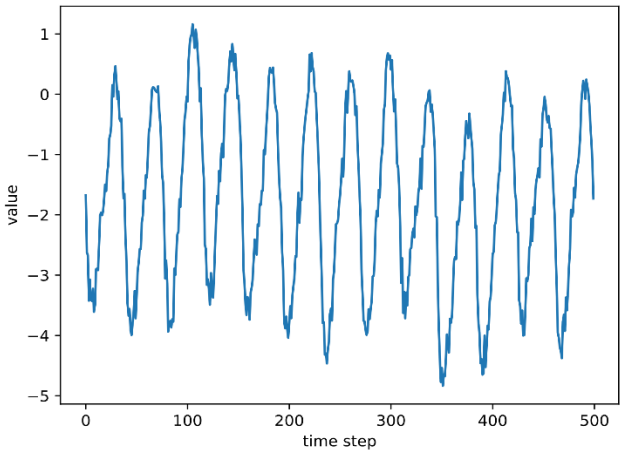

Figure 6. Dynamics of the latent vector for all time steps (AE1).

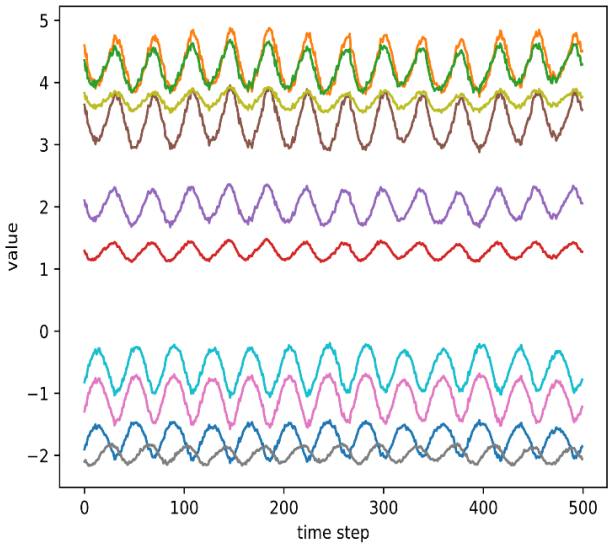

Figure 7. Dynamics of the latent vector for all time steps (AE10). The different lines plotted correspond to the temporal evolution of every variable in the latent vector.

Every image has dimension $(256 \times 128 \times 2)$, where 2 represents the number of channels (1 channel for every velocity component).

A predicted pixel matches with the original pixel if the relative error between X and X' is smaller than a defined tolerance value ϵ, i.e.,

$$\left|\frac{X'(i,j,k) - X(i,j,k)}{X(i,j,k)}\right| \times 100 < \epsilon, \tag{3}$$

where i, j, and k represent the indices of the corresponding pixel.

In Tab. 1, the average accuracy is measured for different tolerance values and its sensitivity to the dimension of the latent vector is performed. AE10 means that the corresponding latent vector is assigned to have 10 variables.

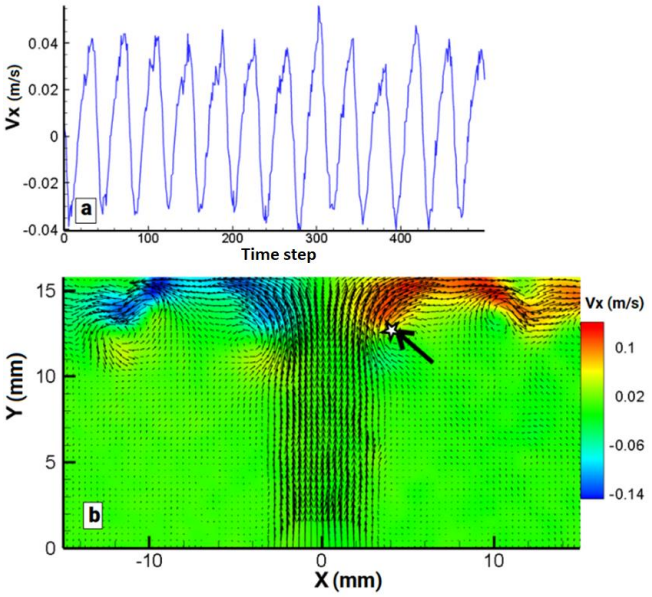

Figure 8. a) Temporal evolution of the transverse velocity at a specific location corresponding to the passage of vortices. b) Snapshot of the flow field showing the location of the tracked point.

Table 1. Average accuracy achieved for all frames using different dimensions of the latent vector. The accuracy is measured using (3) for different tolerance value ϵ.

Accuracy (%)	AE10	AE5	AE1
Tolerance 1%	95.617	95.613	78.970
Tolerance 2%	99.394	99.330	99.053
Tolerance 5%	99.824	99.824	99.846

Results show that, if tolerance is fixed to be 2%, with only 1 variable in the latent vector we can effectively reproduce the flow field image using the AE1 with a reduction to 0.0015% in size. Fig. 4 shows a comparison between the original image and the model at a given time step using AE1.

Fig. 5 presents the matched pixels (shown in red) between the original images and the models with a 2% tolerance level. The results for AE1 (latent vector comprising one variable) and AE10 (latent vector comprising ten variables) are presented in this figure. It can be observed that in both AE1 and AE10, whether for Vx or Vy, the mismatched pixels identified in blue color are mainly obtained in the region of radial flow after the jet impinges on the wall. It can be also noted that the mismatch is more significant for Vy. This zone corresponds to the flow separation region, as discussed by El Hassan et al., 2013.

Figs. 6 and 7 show the latent vector dynamics for both AE1 and AE10 cases throughout all time steps. A sinusoidal pattern is shown in all variables; we conjecture these variations are related to the passages of vortices. Fig. 8(a) shows the transverse velocity (Vx) obtained from a specific point (marked at the top of the arrow in Fig. 8(b)) where the vortices pass. The transverse velocity evolution, which directly correlates with vortex passages, exhibits a sinusoidal pattern.

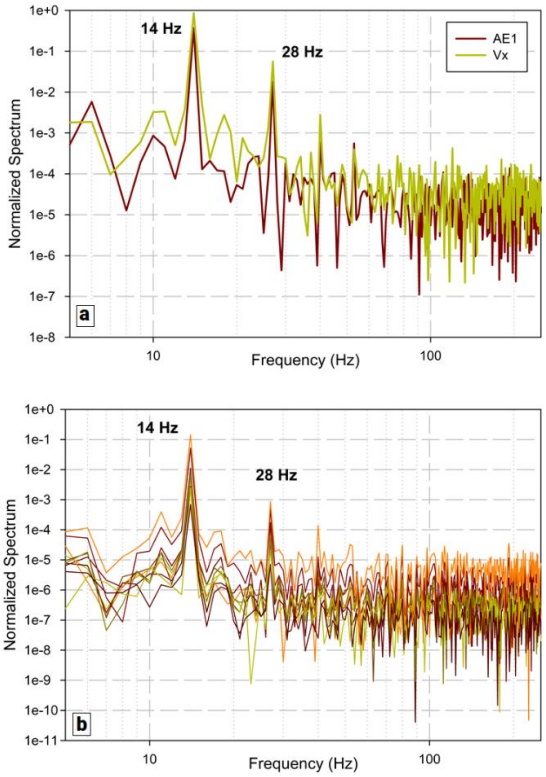

Figure 9. Spectra of: (a) Variable of the latent vector of AE1 and transverse velocity Vx, (b) Variables of the latent vector of AE10.

In order to examine the correlation between the sinusoidal variation of the latent vector in both cases AE1 and AE10, the spectral content of the AEs variables and the transverse velocity are plotted in Fig. 9(a). It can be seen that AE1 and Vx exhibit two dominant frequency peaks at $F = 14$ Hz and its harmonic at $2 \times F$. Fig. 9(b) illustrates the spectra of the 10 variables of the latent vector of AE10, showing a similar observation of the two frequency peaks at 14 and 28 Hz. These findings reveal the association between the AE variables and the vortical structures.

5. Conclusion

In this study, the vortex dynamics of an impinging jet were investigated using AEs, which are a type of convolutional neural networks that are here used to learn about the principal features of the flow. Velocity fields were acquired using a Particle Image Velocimetry (PIV) system at a Reynolds number of Re = 1260.

The results showed that the flow field image can be effectively reproduced using the AE with small number of variables in the latent vector. Additionally, the spectral content of the AE variables presented two main peaks of frequency that were the same as those found in the spectrum of the transverse velocity extracted

where the main vortices pass. This indicates a correlation between the AE variables and the vortical structures.

While the developed model shows accurate results, it is important to consider the presenting limitations. Despite that the identified correlation between the hidden features learned and the transverse velocity is promising; further analysis is needed to understand the physical meaning of these variables. In addition, the analysis relies on the availability and representativeness of experimental or simulation data for representing the flow behavior.

Based on these findings, it is obvious that the prediction is working better in the regions where the flow is periodic. The prediction errors are mainly located in the flow separation regions for Vy. This opens the door to further analysis and improvement to the model used. Efforts should be focused on improving the model for more accurate prediction in the flow separation regions. Furthermore, we aim to extend the presented framework to include additional input parameters, such as the Reynolds number, to predict the corresponding flow field. Additionally, a model could be developed to predict the flow dynamics based on one sensor input, such as wall shear stress variation. Such a model could allow us, based on the flow dynamics, to predict heat transfer and energy savings in many applications.

References

Amsallem, D., & Farhat, C. (2008). Interpolation Method for Adapting Reduced-Order Models and Application to Aeroelasticity. AIAA Journal, 46(7), 1803–1813. https://doi.org/10.2514/1.35374

Assoum, H. H., El Hassan, M., Abed-Meraim, K., & Sakout, A. (2014). The vortex dynamics and the self sustained tones in a plane jet impinging on a slotted plate. European Journal of Mechanics - B/Fluids, 48, 231–235. https://doi.org/10.1016/j.euromechflu.2014.06.008

Assoum, H. H., Hamdi, J., Abed-Meraïm, K., El Hassan, M., Hammoud, A., & Sakout, A. (2017). Experimental investigation the turbulent kinetic energy and the acoustic field in a rectangular jet impinging a slotted plate. Energy Procedia, 139, 398–403. https://doi.org/10.1016/j.egypro.2017.11.228

Assoum, H. H., Hamdi, J., Hassan, M. E., Abed-Meraim, K., Kheir, M. E., Mrach, T., Asmar, S. E., & Sakout, A. (2020). Turbulent kinetic energy and self-sustaining tones: Experimental study of a rectangular impinging jet using high Speed 3D tomographic Particle Image Velocimetry. Journal of Mechanical Engineering and Sciences, 14(1), 6322–6333. https://doi.org/10.15282/jmes.14.1.2020.10.0495

Benner, P., Gugercin, S., & Willcox, K. (2015). A Survey of Projection-Based Model Reduction Methods for Parametric Dynamical Systems. SIAM Review, 57(4), 483–531. https://doi.org/10.1137/130932715

Berner, M. O., Scherer, V., & Mönnigmann, M. (2020). Controllability analysis and optimal control of biomass drying with reduced order models. Journal of Process Control, 89, 1–10. https://doi.org/10.1016/j.jprocont.2020.03.002

Deane, A. E., Kevrekidis, I. G., Karniadakis, G. E., & Orszag, S. A. (1991). Low-dimensional models for complex geometry flows: Application to grooved channels and circular cylinders. Physics of Fluids A: Fluid Dynamics, 3(10), 2337–2354. https://doi.org/10.1063/1.857881

El Hassan, M., Assoum, H. H., Sobolik, V., Vétel, J., Abed-Meraim, K., Garon, A., & Sakout, A. (2012). Experimental investigation of the wall shear stress and the vortex dynamics in a circular impinging jet. Experiments in Fluids, 52(6), 1475–1489. https://doi.org/10.1007/s00348-012-1269-5

El Hassan, M., Assoum, H., Martinuzzi, R., Sobolik, V., Abed-Meraim, K., & Sakout, A. (2013). Experimental investigation of the wall shear stress in a circular impinging jet. Physics of Fluids, 25(7), 077101.

Eng Ewe, W., Fudholi, A., Sopian, K., Solomin, E., Hossein Yazdi, M., Asim, N., Fatima, N., Pikra, G., Sudibyo, H., Fatriasari, W., Heru Kuncoro, A., Supriyadi Ali Nandar, C., & Abimanyu, H. (2022). Jet impingement cooling applications in solar energy technologies: Systematic literature review. Thermal Science and Engineering Progress, 34, 101445. https://doi.org/10.1016/j.tsep.2022.101445

Fabris, D., Liepmann, D., & Marcus, D. (1996). Quantitative experimental and numerical investigation of a vortex ring impinging on a wall. Physics of Fluids, 8(10), 2640–2649. https://doi.org/10.1063/1.869049

John, T., Guay, M., Hariharan, N., & Naranayan, S. (2010). POD-based observer for estimation in Navier–Stokes flow. Computers & Chemical Engineering, 34(6), 965–975. https://doi.org/10.1016/j.compchemeng.2009.12.001

Lumley, J. L. (1967). The structure of inhomogeneous turbulent flows. Atmospheric Turbulence and Radio Wave Propagation, 166–178.

Maulik, R., Lusch, B., & Balaprakash, P. (2021). Reduced-order modeling of advection-dominated systems with recurrent neural networks and convolutional autoencoders. Physics of Fluids, 33(3), 037106. https://doi.org/10.1063/5.0039986

Orlandi, P., & Verzicco, R. (1993). Vortex rings impinging on walls: Axisymmetric and three-

dimensional simulations. Journal of Fluid Mechanics, 256, 615–646. https://doi.org/10.1017/S0022112093002903

Pawar, S., Rahman, S. M., Vaddireddy, H., San, O., Rasheed, A., & Vedula, P. (2019). A deep learning enabler for nonintrusive reduced order modeling of fluid flows. Physics of Fluids, 31(8), 085101. https://doi.org/10.1063/1.5113494

Reineking, L., Sommer, K., Ravichandran, Y. P., Skoda, R., & Mönnigmann, M. (2022). Long-term stable reduced models for hydraulic systems governed by Reynolds averaged Navier-Stokes equations. IFAC-PapersOnLine, 55(7), 254–259. https://doi.org/10.1016/j.ifacol.2022.07.453